Research Paper

Photocatalytic CO_2 reduction over V and W codoped TiO_2 catalyst in an internal-illuminated honeycomb photoreactor under simulated sunlight irradiation

Zhuo Xiong [a], Ze Lei [a], Siming Ma [a], Xiaoxiang Chen [a], Bengen Gong [a], Yongchun Zhao [a,*], Junying Zhang [a], Chuguang Zheng [a], Jeffrey C.S. Wu [b,*]

[a] State Key Laboratory of Coal Combustion, School of Energy and Power Engineering, Huazhong University of Science & Technology, 1037 Luoyu Road, Wuhan 430074, China
[b] Department of Chemical Engineering, National Taiwan University, No. 1, Section 4, Roosevelt Road, Taipei 10617, Taiwan

ARTICLE INFO

ABSTRACT

In this paper, V and W codoped TiO_2 catalysts were prepared and coated on the surface of honeycomb support. The V^{4+} doped in TiO_2 lattice enhanced the visible light absorption of TiO_2 while the V_2O_5 on the surface of TiO_2 and W^{6+} in TiO_2 lattice could trap photogenerated electrons and transfer them to CO_2 and water adsorbed on the surface of catalyst, resulting in effective separation of photogenerated charges. CO_2 photocatalytic reduction over V and W codoped TiO_2 catalyst was conducted in an internal-illuminated honeycomb photoreactor under simulated sunlight irradiation. Due to the strong visible light absorption and effective separation of photogenerated charges caused by V and W codoping and stable chemical states of V and W during photocatalytic reaction, the V and W codoped TiO_2 catalysts exhibited stable and enhanced photocatalytic activity comparing with pristine TiO_2 and single metal doped TiO_2.

© 2017 Elsevier B.V. All rights reserved.

1. Introduction

Global warming and energy shortage are two major problems which the world is facing nowadays. One of the best solutions to the above issues is to convert greenhouse gas (mainly CO_2) into solar fuels, which can mitigate global warming and provide valuable fuels simultaneously [1–3]. Since Inoue et al. [4] first reported CO_2 photocatalytic reduction on semiconductors in 1979, a variety of semiconductors such as TiO_2 [5–7], ZnO [8,9], CeO_2 [10,11], C_3N_4 [12], and WO_3 [13,14] have been applied for CO_2 photocatalytic reduction. Among them, TiO_2 is one of the most promising photocatalysts due to its high activity, good photostability, low cost, and environmental friendliness [15–17]. However, TiO_2 still suffers from low reaction efficiency, low utilization of visible light, fast recombination of photogenerated electron-hole pairs, and wide band gap (3.2 eV) [18–20].

It has been reported that doping foreign atoms into TiO_2 can effectively improve the photocatalytic activity of TiO_2 because the dopants can promote the separation of photogenerated charges and extend the light absorption region towards visible light [21,22]. For example, Wu et al. [23] reported that V doping narrowed the band gap of TiO_2 and effectively enhanced the activity of V doped TiO_2 catalyst. Tahir [24] found that In doping could effectively inhibited the recombination of photogenerated charges and enhanced the photocatalytic activity of TiO_2 for CO_2 reduction. Recently, codoping has been recognized to be a more useful approach to improve the photocatalytic activity of TiO_2 than single element doping due to the synergy of different dopants [22,25]. Many different elements including V-N [26], V-Ag [27], W-C [25] and Mo-C [28] were combined and codoped into TiO_2 to improve its photocatalytic activity. In our previous work [29], we found that W doped TiO_2 exhibited high photocatalytic activity under UV light irradiation while V doping greatly enhanced the visible light activity of TiO_2. Thus, it is possible to achieve a highly efficient visible-light driven photocatalyst by codoping V and W into TiO_2. However, few studies have considered the effect of V and W codoping on the photocatalytic CO_2 reduction of TiO_2.

The type of reactor and catalyst support is also important in CO_2 photocatalytic reduction. Maximizing the surface of catalyst and utilization of light are imperative to enhance the efficiency of CO_2 photocatalytic reduction. Recently, Liou et al. [30] reported an internally illuminated monolith photoreactor with distributed optical fibers inside the channels of the monolith. The monolith could ensure the large surface area of catalyst while the optical
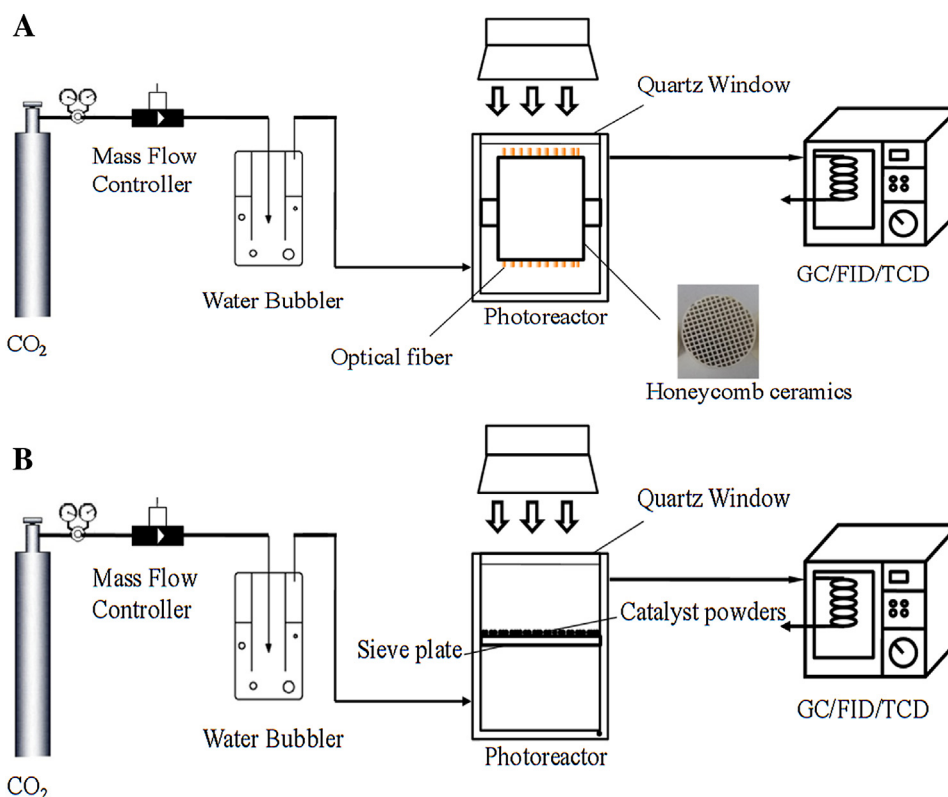

Fig. 1. Schematic diagrams of the internal-illuminated honeycomb reactor (A) and the conventional powder reactor (B).

fibers could transport enough light to the catalyst coated on the monolith [31], resulting in higher efficiency of CO_2 photocatalytic reduction than other types of reactors [32]. Similarly, Tahir et al. [33] reported enhanced CO_2 photocatalytic reduction over Ni and In codoped TiO_2 in a monolith reactor.

In this work, V and W doped TiO_2 catalysts were synthesized and coated on the surface of honeycomb internal channels. The effect of V and W doping on the physico-chemical property and CO_2 photocatalytic reduction activity of TiO_2 was investigated in an internal-illuminated honeycomb photoreactor. The roles of V and W were discussed in the CO_2 photocatalytic reduction. Finally, a possible mechanism of CO_2 photocatalytic reduction was proposed over V and W doped TiO_2 catalyst.

2. Experimental

2.1. Catalyst preparation and coating process

The TiO_2 sol was prepared through a controlled thermal hydrolysis method [31] with slight modification. In a typical process, 87.6 g of titanium butoxide was slowly added into 510 mL of HNO_3 aqueous solution (0.1 M) under vigorous stirring. The mixture was kept stirring at 80 °C for 8 h to obtain clear TiO_2 sol. Then, 10 g of PEG (Mw = 20000) was added to improve the viscosity of TiO_2 sol for dip-coating. The metal/TiO_2 sol was prepared by dissolving a certain amount of metal precursors in the TiO_2 sol. For V/TiO_2 sol, a certain amount of vanadyl (IV) acetylacetonate was dissolved in methanol and then the mixture was added in the TiO_2 sol. For W/TiO_2 sol, ammonium tungstate hydrate was dispersed in oxalic acid aqueous solution before adding into the TiO_2 sol. The V-W/TiO_2 sol was prepared by adding both V and W precursors into the TiO_2 sol.

The cordierite honeycomb support used for catalyst carrier was purchased from the Chauger honeycomb support company (Taiwan). Each honeycomb support is 4 cm in diameter and has 160 square channels (2×2 mm). The metal/TiO_2 catalyst was coated on the honeycomb support by the method reported in the literature [30]. The honeycomb support was immersed into the metal/TiO_2 sol and soaked for 30 min. Then the honeycomb support was taken out of the sol and the excess sol was blown away using compressed air. Finally, the resultant honeycomb was calcined in air at 500 °C for 2 h (1 °C/min). The V, W codoped TiO_2 catalysts were denoted as VxWyT (x% and y% are the mass ratios of V_2O_5/TiO_2 and WO_3/TiO_2 in the catalysts, respectively). Powder catalysts were also prepared in the same procedure for comparison.

2.2. Catalyst characterization

X-ray diffraction (XRD) patterns of the catalysts were recorded on an Empyrean diffractometer using Cu Kα radiation ($\lambda = 0.1542$ nm) in the range of 10−80°. The surface morphology and elemental mapping of the catalysts were examined by environment scanning electron microscopy (ESEM) with an FEI Quanta 200 instrument. Transmission electron microscopy (TEM) images of the catalysts were obtained by using an FEI Tecnai G^2 F30 instrument. The specific surface areas and pore size distribution of the catalysts were measured by a Micrometrics ASAP 2020 surface area and porosity analyzer. X-ray photoelectron spectra (XPS) of the catalysts were recorded on a Shimadzu/KRATOS AXIS-ULTRA DLD-600W instrument equipped with Al/Mg Kα radiation. Photoluminescence (PL) and Raman spectra of the catalysts were recorded on a confocal laser Raman microscope (Horiba JobinYvon, LabRAM HR800) by using a 325 nm and a 532 nm excitation light source, respectively. The UV–vis absorbance spectra of the catalysts were measured by a UV–vis spectrophotometer (Perkin Elmer, Lambda 950).
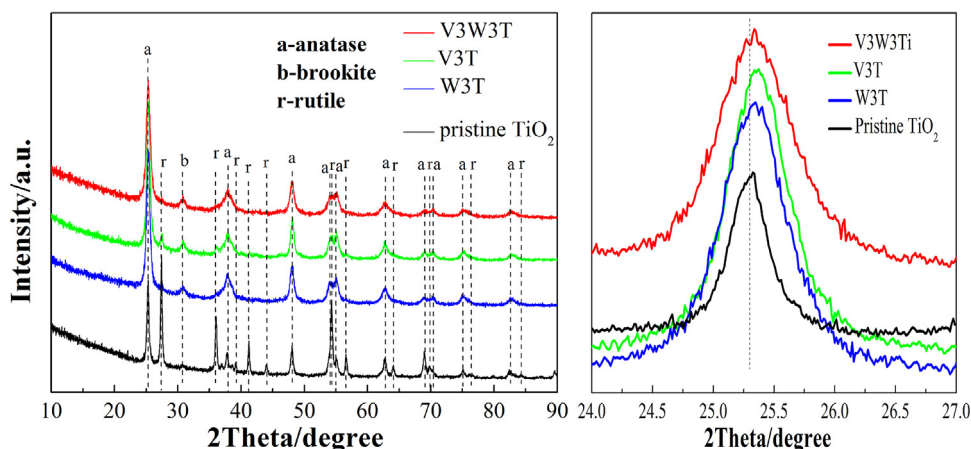
Fig. 2. XRD patterns of as-prepared catalysts.

2.3. Photocatalytic reduction of CO_2

CO_2 photocatalytic reduction under simulated sunlight irradiation (300 nm < λ <400 nm, 18.5 mW cm^{-2}; 400 nm < λ < 800 nm, 44.6 mW cm^{-2}; measured in front of the quartz window) was carried out in a continuous internal-illuminated honeycomb photoreactor (Fig. 1A). The honeycomb support was threaded with commercial communication optical fibers with pure PMMA core and F-doped PMMA cladding. The optical fiber has a diameter of 1 mm. The honeycomb support with optical fibers was placed into a cylindrical Pyrex glass reactor (375 mL), which had a quartz window on the top for light irradiation. The simulated sunlight was supplied by a 300 W xenon lamp. The reactor was heated to 50 °C by using heating tape. Ultra-pure CO_2 (99.999%) passed through a water bubbler to generate a mixture of CO_2 and water vapor (water vapor/CO_2 ratio = 4.4 vol.%). Prior to illumination, the reactor was first purged with CO_2 and water vapor mixture at a flow rate of 200 mL min^{-1} for 1 h and then 10 mL min^{-1} for another 30 min. After the flow was stabilized, the Xe lamp was switched on to start the experiment. The concentrations of H_2, CO, and hydrocarbons in the exhaust gas were analyzed every 15 min by a gas chromatography (GC) equipped with an on-line sampling loop (1 mL), a flame ionization detector (FID), and a thermal conductivity detector (TCD). First, the effluents were pre-separated by a carbon molecular sieve (TDX-01) column to flush CO_2 to atmosphere. Then the effluents flowed through a molecular sieve 5A column for the separation of H_2, O_2, N_2, CH_4, and CO. Finally, H_2 in the effluents was analyzed by the TCD detector and CH_4 and CO (converted to CH_4 by a methanizer) were analyzed by the FID detector. Ar was used as the carrier gas.

For comparison, CO_2 photocatalytic reduction over catalyst powders was also performed in the same cylindrical Pyrex glass reactor (conventional powder reactor, Fig. 1B). The other parts of the reactor are the same as the honeycomb reactor. The catalyst powders were spread on a sieve plate placed in the center of the cylindrical reactor. The amount of catalyst powders was the same as that of catalyst loaded on the honeycomb.

A series of background tests were conducted to confirm that any carbon-containing compounds in the effluent gas measured by the GC indeed originated from CO_2 photoreduction. First, tests were conducted using CO_2 and water vapor as the purging and reaction gases: (1) empty reactor and (2) reactor with honeycomb support without coating. No carbon-containing products were detected in the dark or under UV–vis light irradiation in these two cases. This demonstrated that the CO_2 reduction could not proceed without photocatalyst. Second, instead of CO_2, Ar and water vapor were used as the purging and reaction gases in the presence of coated honeycomb support. No carbon-containing compounds were produced under UV–vis light irradiation. This indicated that the CO_2 was the sole carbon source.

3. Results and discussion

3.1. Characterization of the catalysts

Fig. 2 shows the XRD patterns of pristine TiO_2, V3T, W3T, and V3W3T catalysts. Pristine TiO_2 mainly existed as anatase and rutile TiO_2. A weak peak at around 30.8° can be ascribed to brookite TiO_2 [31]. In the case of V or W doping, the intensity of the peaks corresponding to rutile TiO_2 decreased remarkably. For V3W3T, the peaks corresponding to rutile TiO_2 nearly disappeared, indicating that either V or W doping inhibited the anatase-rutile phase transformation. The average crystalline size of TiO_2 was determined by XRD using the Scherrer equation (as shown in Table 1). The crystalline sizes of V3T, W3T, and V3W3T were all smaller than that of pristine TiO_2, which demonstrated that V and W doping inhibited the growth of TiO_2 grains. Similar results were reported in the literatures [26]. No V or W species were detected by XRD, which can be attributed to the low concentration of V and W doping. It is notable that the anatase (101) peak of V3T, W3T, and V3W3T shifts towards the higher diffraction angle, indicating that V and W ions might incorporate into the lattice of anatase TiO_2 and substituted for Ti^{4+}.

To further confirm the successful doping of V and W into the lattice of TiO_2, Raman spectra of pristine TiO_2, V3T, W3T, and V3W3T are exhibited in Fig. 3. The Raman spectra showed that pristine TiO_2 contained anatase, rutile, and brookite phases (Fig. 3A). The intensity of the Raman peaks corresponding to rutile phase obviously decreased after V or W doping, indicating the formation of rutile phase was inhibited, which is in line with the results of XRD. It is notable that the intensity of Raman peaks of doped TiO_2 samples were much lower than that of pristine TiO_2, indicating the presence of V and W dopants [34,35]. In the magnified Raman spectra (Fig. 3B), it can be seen that the raman peaks of doped TiO_2 samples exhibited a slight blue shift comparing to the pristine TiO_2. This might be attributed to the distortion of crystal lattice structure and the increased Ti-O bond caused by V and W ions [36]. This also demonstrated the successful doping of V and W into the lattice of TiO_2. In Fig. 3C, a small peak at around 285 cm^{-1} was observed on the Raman spectra of both V3T and V3W3T, which is one of the characteristic Raman peaks of V_2O_5 [34]. This indicated that part of the V dopant in V3T and V2W3T exsited as V_2O_5 on the surface of TiO_2.
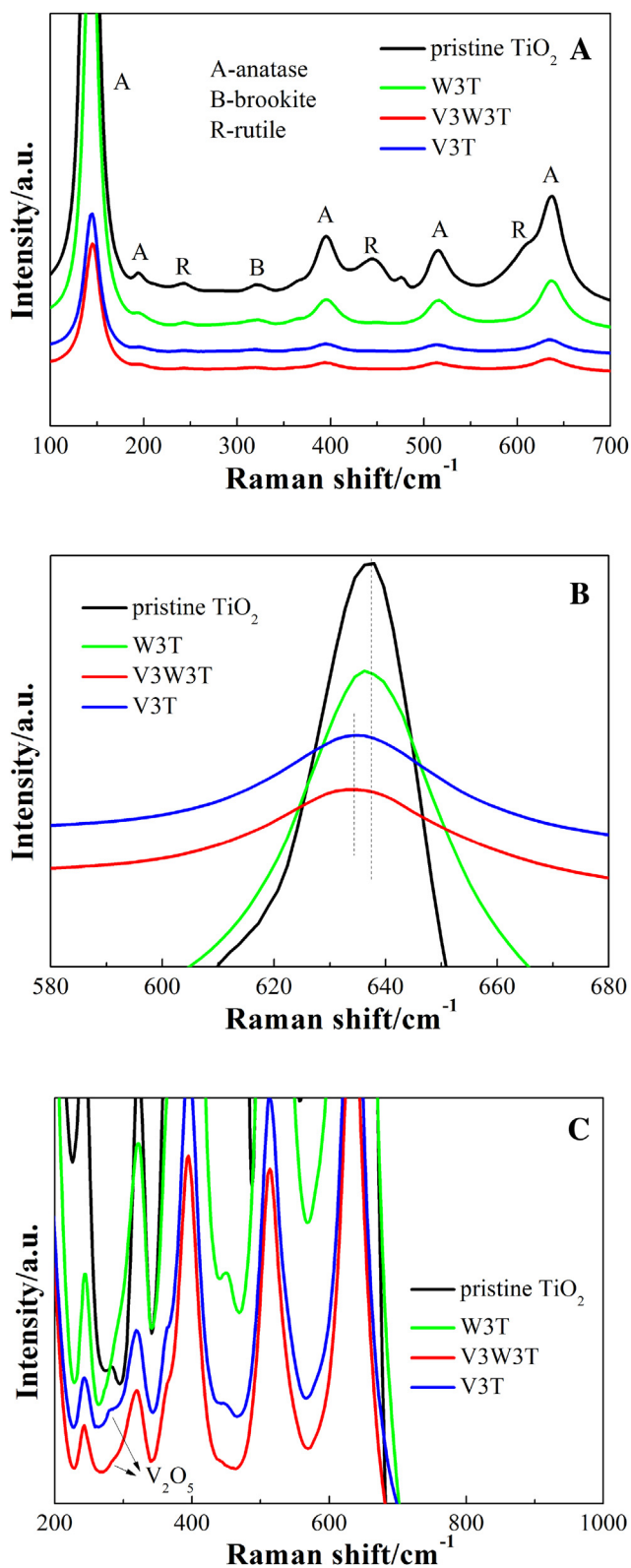
Fig. 3. Raman spectra of pristine TiO$_2$, V3T, W3T, and V3W3T catalysts.
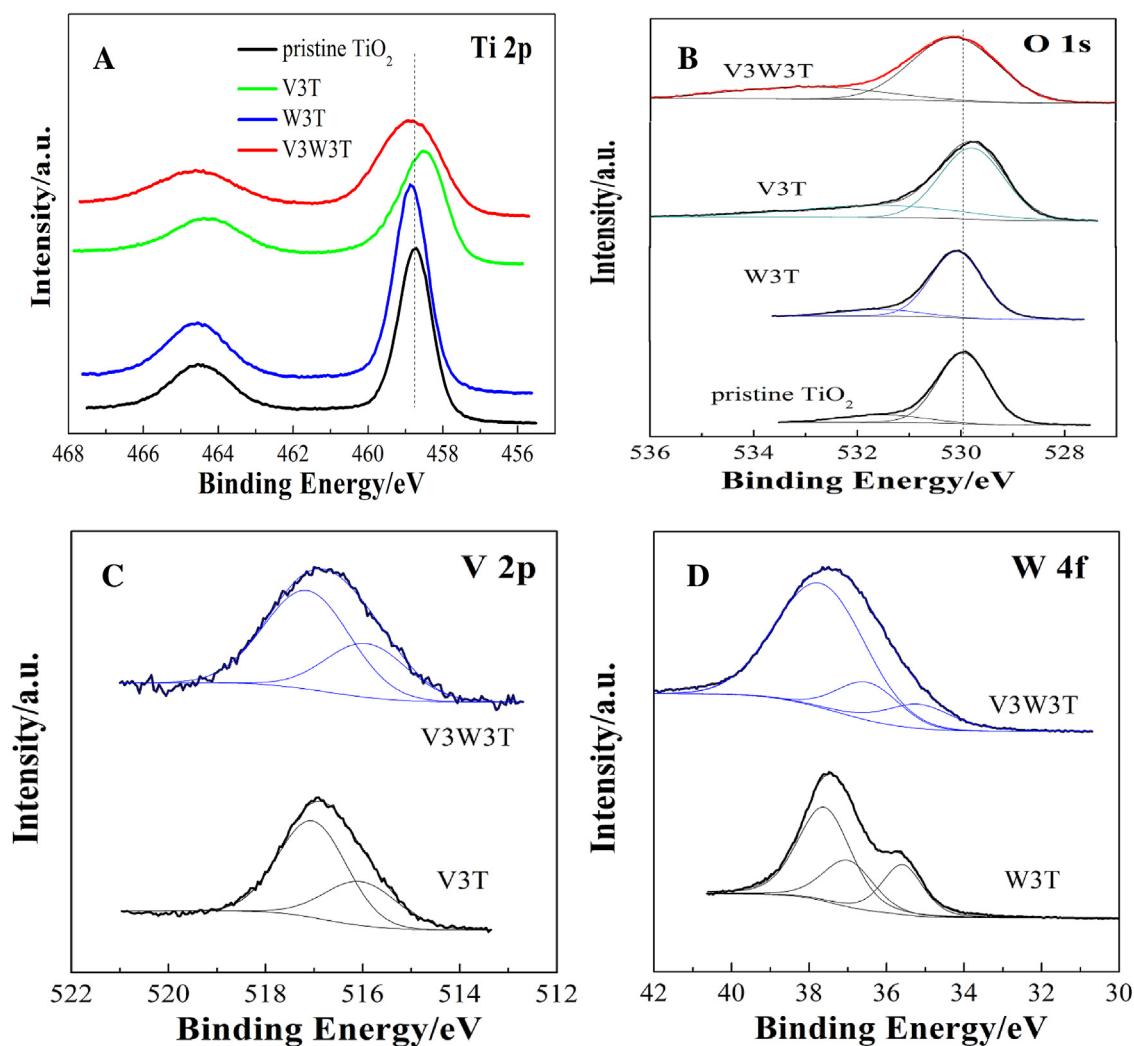
However, no peaks corresponding to WO$_3$ crystals were observed, suggesting that the incorporated W is highly dispersed in TiO$_2$ without forming large crystals [37]. N$_2$ adsorption-desorption was used to explore the textual properties of pristine TiO$_2$, V3T, W3T, and V3W3T catalysts. The BET surface area, pore volume, and pore size of the samples were summarized in Table 1. Both V and W dop-

ing enhanced the surface area of TiO$_2$. V3W3T catalyst possesses the largest surface area (174.8 m^2 g^{-1}) among all the samples. The enhanced surface area can be attributed to the decreased TiO$_2$ crystalline size caused by V and W doping, as evident by XRD analysis (Table 1).

Table 1
Crystalline size, surface area, pore volume, and pore size of the powder samples.

Samples	Crystalline size[a] /nm	Band gap /eV	BET surface area /m^2 g^{-1}	Pore volume /cm^3 g^{-1}	Pore size /nm
Pristine TiO$_2$	25.1	3.00	13.6	0.030	8.8
V3T	19.1	3.01	53.7	0.122	9.1
W3T	15.4	2.29	62.4	0.120	7.7
V3W3T	14.0	2.31	174.8	0.134	3.1

[a] calculated by Scherrer's equation.

Fig. 4. Ti 2p (A), O 1s (B), V 2p (C) and W 4f (D) XPS spectra of the samples.

XPS was used to investigate the chemical states of Ti, O, V and W on the surface of the catalysts. Fig. 4A shows the high-resolution Ti 2p XPS spectra of the samples. There exist two peaks in the binding energy region of Ti 2p. The binding energies of Ti 2p$_{3/2}$ for pristine TiO$_2$ and W3T are around 458.6 eV, which indicates Ti^{4+} in pristine TiO$_2$ and W3T [38,39]. Notably, comparing with pristine TiO$_2$, the binding energy of Ti 2p$_{3/2}$ for V3T shifted to a negative value, suggesting that some of Ti^{4+} is reduced to Ti^{3+}. This phenomenon can be attributed to the substitution of Ti^{4+} by the doped V^{4+} and the formation of Ti-O-V bonds [26,40], which could induce defects in the TiO$_2$ lattice, leading to the reduction of Ti^{4+} into Ti^{3+} or the formation of oxygen vacancies [27]. The formation of Ti^{3+} in V doped TiO$_2$ were also observed by Pham et al. [27] and Wang et al. [36] and they owed it to the incorporation of vanadium ions into the TiO$_2$ lattice. However, for V3W3T, the Ti 2p binding energy shifted back to around 458.6 eV. This indicated that W doping inhibited

the reduction of Ti^{4+}. The high-resolution O 1s XPS spectra of all the samples in Fig. 4B can be resolved into two peaks. The one with lower energy is assigned to oxygen in TiO$_2$ lattice (O$_L$) and the other one can be ascribed to superficial oxygen of hydroxyl species (O$_H$) [17]. The binding energy of O 1s peak for V3T is also lower than that of pristine TiO$_2$, indicating the electron transfers from V to TiO$_2$.

Fig. 4C shows the high-resolution V 2p XPS spectra of V3T and V3W3T catalysts, which can be resolved into two peaks. The peak at around 517.0 eV could be ascribed to V^{5+} [26], whereas that at around 515.8 eV was assigned to V^{4+} [27]. Combining the results of XRD and Raman spectra, V^{4+} ions could substitute for Ti^{4+} ions to form a Ti-O-V bond in the TiO$_2$ lattice while the V^{5+} could exist in the form of V$_2$O$_5$ on the surface of TiO$_2$, resulting from much closer radii between Ti^{4+} (74.5 pm) and V^{4+} (72.0 pm) than V^{5+} (68.0 pm) [36]. Similar results have also been reported by other researchers [27,41,42]. The concentration of V^{5+} was much higher than that of
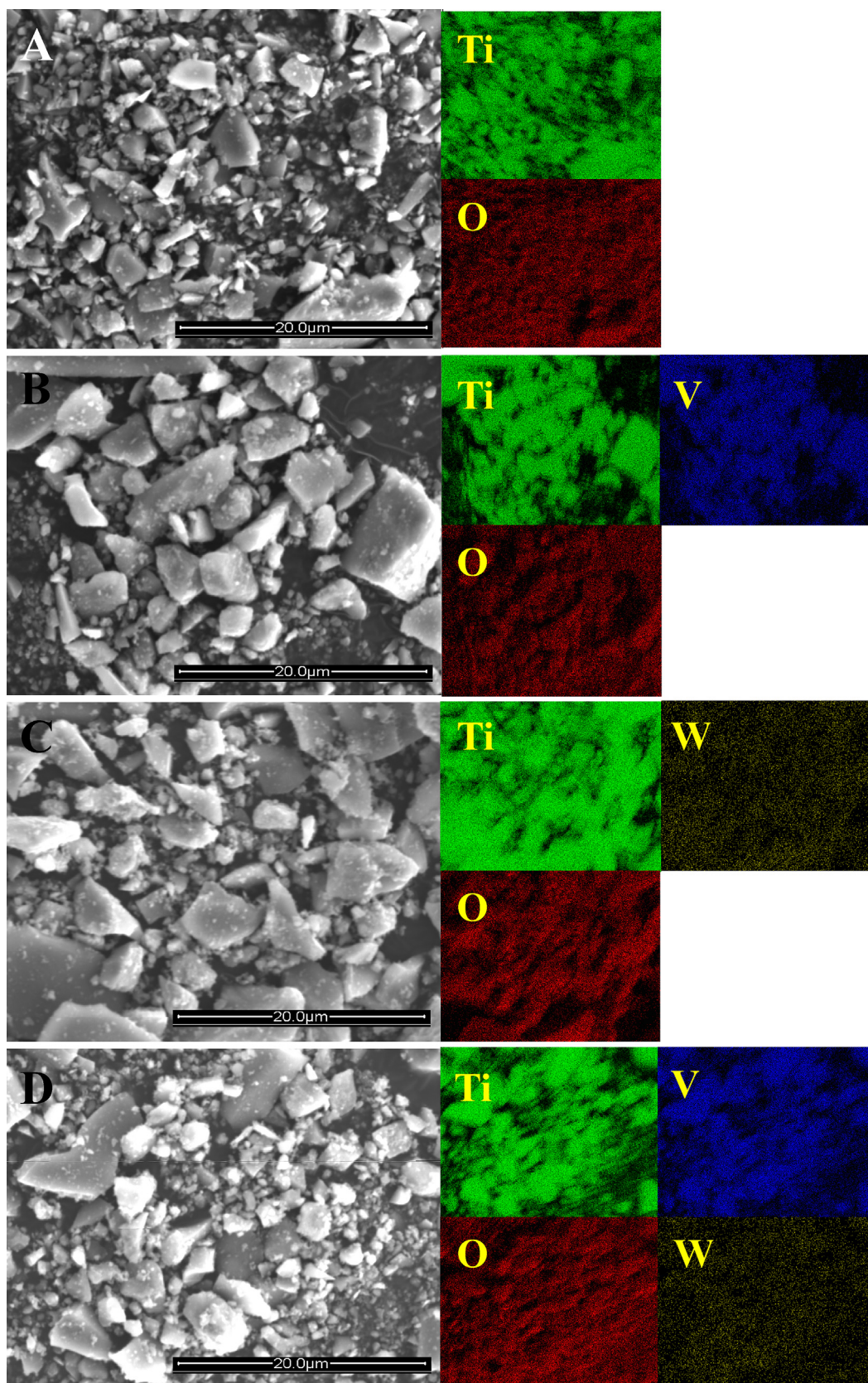
Fig. 5. SEM images and elemental mapping of pristine TiO_2 (A), V3T (B), W3T(C), and V3W3T (D).

V^{4+} for both V3T and V3W3T catalysts, demonstrating that V^{5+} was dominant on the surface of V3T and V3W3T catalyst. In addition, W doping does not show obvious influence on the chemical state of V. The W 4f region displays two peaks at 37.4 and 35.4 eV (Fig. 4D), which can be ascribed to the W $4f_{5/2}$ and W$4f_{7/2}$ for W^{6+} [43]. The peak at around 37.0 eV can be assigned to Ti 3p [44]. Considering the
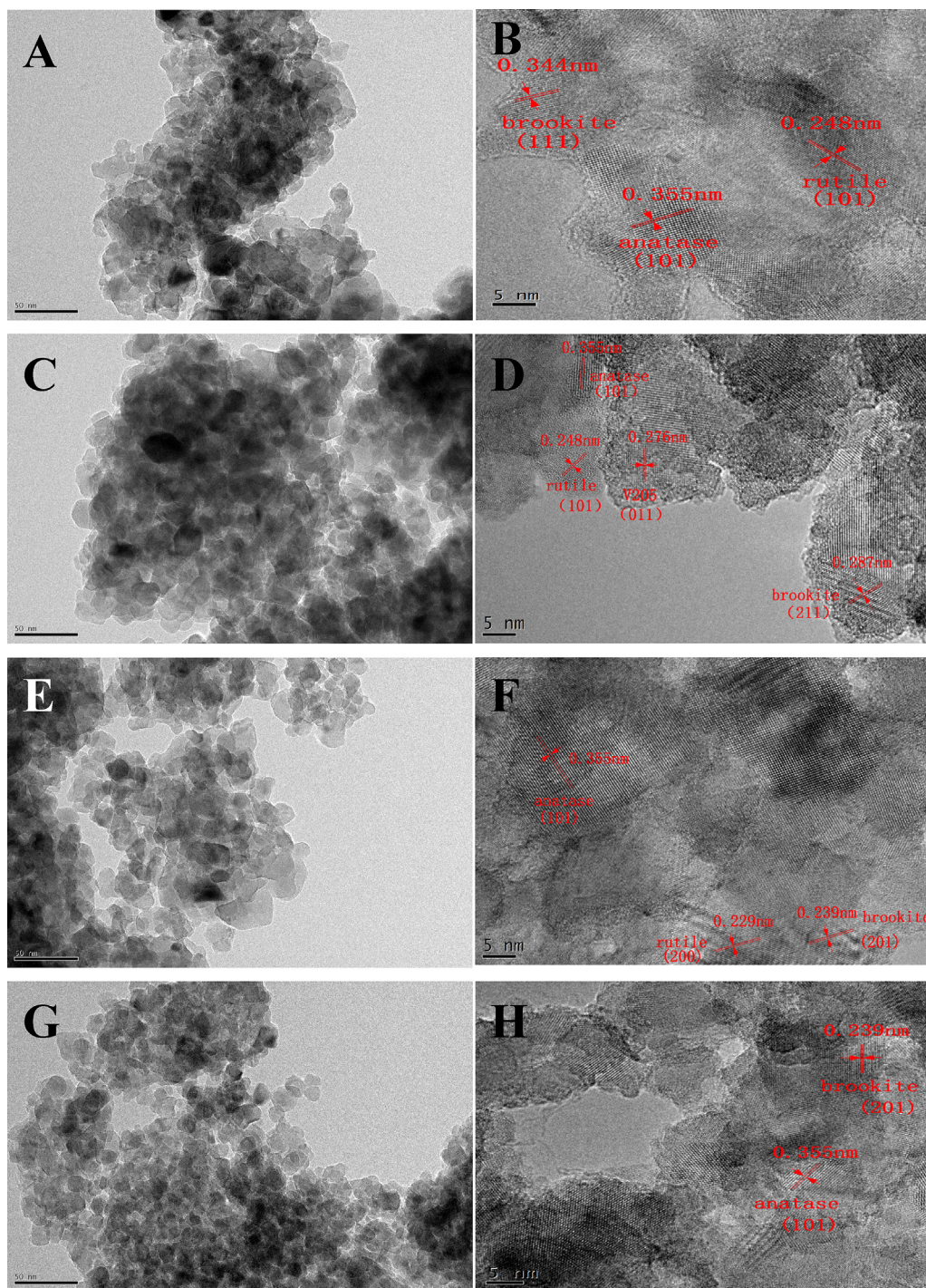
Fig. 6. TEM and HR-TEM images of pristine TiO$_2$ (A, B), V3T (C, D), W3T(E, F), and V3W3T (G, H) catalysts.

similar radii between Ti^{4+} (74.5 pm) and W^{6+} (74.0 pm), W^{6+} could be doped into the lattice of TiO$_2$ and substituted for Ti^{4+} according to the XRD results. The chemical state of W was not affected by V doping.

The SEM images of the catalysts in Fig. 5 show that V or W doping has no significant influence on the morphology of TiO$_2$ catalyst. In addition, elemental mapping exhibited uniform distribution of V and W in TiO$_2$. Fig. 6 illustrates the TEM and HR-TEM images of pristine and doped TiO$_2$ catalysts. It is notable that a similar morphology could still be obtained by V or W doping. The average size of TiO$_2$ particles is around 20 nm. For pristine TiO$_2$, V3T, and W3T, TiO$_2$ existed in the form of anatase, rutile, and brookite according to

the interplanar spacing showing in the HR-TEM images. No rutile TiO$_2$ nanoparticle was observed in the HR-TEM image of V3W3T (Fig. 6H), which is in line with the results of XRD that the formation of rutile TiO$_2$ phase was inhibited by V and W doping. V$_2$O$_5$ particles were observed in the HR-TEM image of V3T (Fig. 6D), which is accordance with the results of XPS analysis that V^{5+} existed as V$_2$O$_5$ on the surface of TiO$_2$. No W species were observed in the TEM images of W3T and V3T3W due to the low concentration of W doping or high dispersion of W species in the catalysts.

The UV–vis absorbance spectra of the catalysts are shown in Fig. 7A. The absorption edges of V3T and V3W3T catalysts exhibited red shift compared to that of pristine TiO$_2$ and W3T, indicating
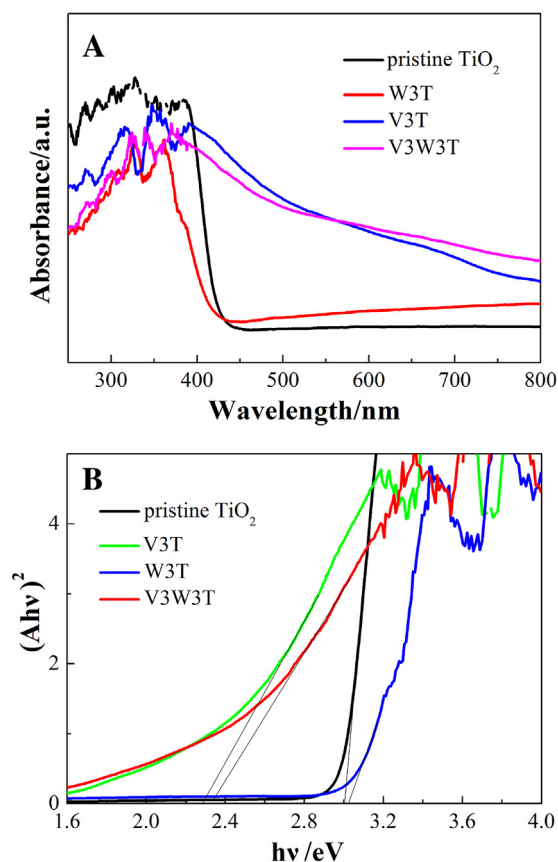
Fig. 8. PL spectra of pristine TiO_2, V3T, W3T and V3W3T catalysts.

Fig. 7. UV–vis absorbance spectra (A) and energy band gap (B) of the catalysts.

centers to reduce the recombination process and favor the separation of photogenerated charges [43]. When the electrons in the VB of TiO_2 are excited to the CB and they will captured by V_2O_5 on the surface of TiO_2 and W^{6+} doped in the lattice of TiO_2 [26,44]. then these trapped electrons can react with CO_2 and water adsorbed on the surface of the catalyst. Therefore, we believe that the decreased PL intensity is due to the effective separation of photogenerated electron-hole pairs caused by V and W doping, which is beneficial for the enhancement of photocatalytic activity.

3.2. Characterization of TiO_2 coated honeycomb support

Fig. 9 shows the photographs of bare and catalyst-coated honeycomb support. The color of honeycomb support changed after coating, implying loading of catalysts. The SEM images and EDS analysis of bare and pristine TiO_2 coated honeycomb support are exhibited in Fig. 10. As shown in Fig. 10A, the bare honeycomb support consisted of cordierite particles. For TiO_2 coated honeycomb support (Fig. 10B), the surface of honeycomb support was cover by a layer of smooth material, which was determined to be TiO_2 according to EDS analysis. This indicated successful loading of TiO_2 catalysts on the honeycomb support.

Fig. 11 illustrates the SEM images and corresponding EDS analysis of the cross-section of TiO_2 coating layer on the honeycomb support. Obviously, many pores can be observed on the cross-section of honeycomb support, while the first 30 μm thick has a higher density, which can be attributed to the coating layer. The EDS line mapping exhibits most Ti element was distributed from 0 to 30 μm deep, indicating the coating thickness was ca. 30 nm. This further indicated successful coating of TiO_2 catalyst on the honeycomb support.

3.3. CO_2 photocatalytic reduction

CO_2 photocatalytic reduction over V3W3T catalyst under simulated sunlight irradiation was performed in the honeycomb reactor and conventional reactor, respectively. Fig. 12 shows the CO, CH_4, and H_2 yields in the above two cases. As shown in Fig. 12, the yields of products from honeycomb reactor were much higher than those from conventional reactor. This can be attributed to the high surface area per unit volume provided by the honeycomb support and efficient utilization of light irradiation via optical fibers [30,31].

Fig. 13 and Table 2 shows the effect of V and W doping on the photocatalytic CO_2 reduction activity and quantum efficiency of TiO_2 catalyst in the honeycomb reactor. H_2, CO, and CH_4 were found to be the main products and CO was dominant among all the products. The activity of pristine TiO_2 was lowest among all

V doping could enhance the visible light absorption of TiO_2. The band gap of the samples was calculated by using $(Ah\nu)^n = k(h\nu - E_g)$, where A is the absorbance, k is the parameter that related to the effective masses associated with the valence and conduction bands, n is 2 for an indirect transition, $h\nu$ is the absorption energy, and E_g is the band gap [5]. Fig. 7B shows the function of $(Ah\nu)^2$ to $h\nu$, and E_g of the samples was summarized in Table 1. The band gap of pristine TiO_2 was lower than that of anatase TiO_2 (3.2 eV) due to the smaller band gap of rutile TiO_2 than anatase TiO_2 [45]. The band gap of V3T is smaller than that of pristine TiO_2, which can be attributed to the formation of an intermediate state below the bottom of CB of TiO_2 caused by V^{4+} doping [26]. Because of the intermediate state within the band gap, the electrons in the VB of TiO_2 can be excited to the intermediate state by absorbing visible light, resulting in enhanced visible light absorption of V doped TiO_2. Nevertheless, the band gaps of W3T and V3W3T were very close to pristine TiO_2 and V3T catalyst, respectively. Although W doping could enhance the visible light absorption of anatase TiO_2 [43,44], it inhibited the formation of rutile TiO_2. As a result, the band gap of pristine TiO_2 and V3T changed very little after W doping.

The PL spectra of the catalysts are shown in Fig. 8. Notably, the intensity of PL spectra of V3T and W3T were both lower than that of pristine TiO_2, indicating that both V and W doping could effectively decrease the recombination of photogenerated electron-hole pairs. The intensity of PL spectra for V3W3T were the lowest one among all the samples, revealing the most effective separation of photogenerated charges over V3W3T catalyst. This phenomenon can be explained as follows, the V_2O_5 on the surface of TiO_2 is a kind of semiconductor and combining it with TiO_2 can form a heterojunction, which can promote the separation of photogenerated electrons and holes and reduce the charge recombination process [34]. The W^{6+} doped in TiO_2 lattice can work as charge-trapping
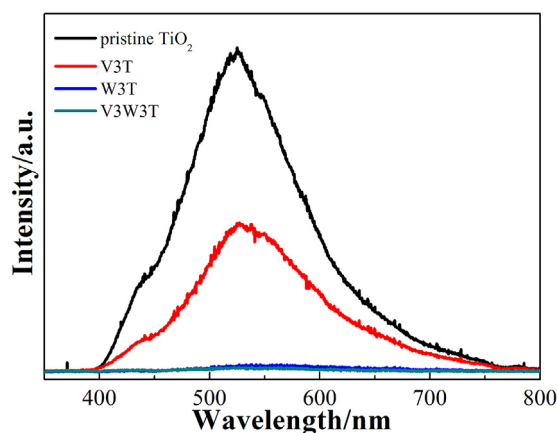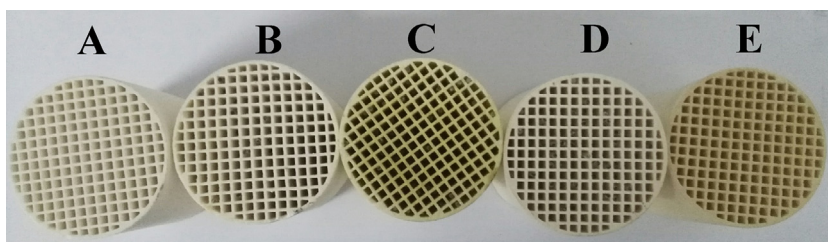
Fig. 9. Photographs of clean (A), pristine TiO$_2$ (B), V3T (C), W3T (D), and V3W3T (E) coated honeycomb ceramics.
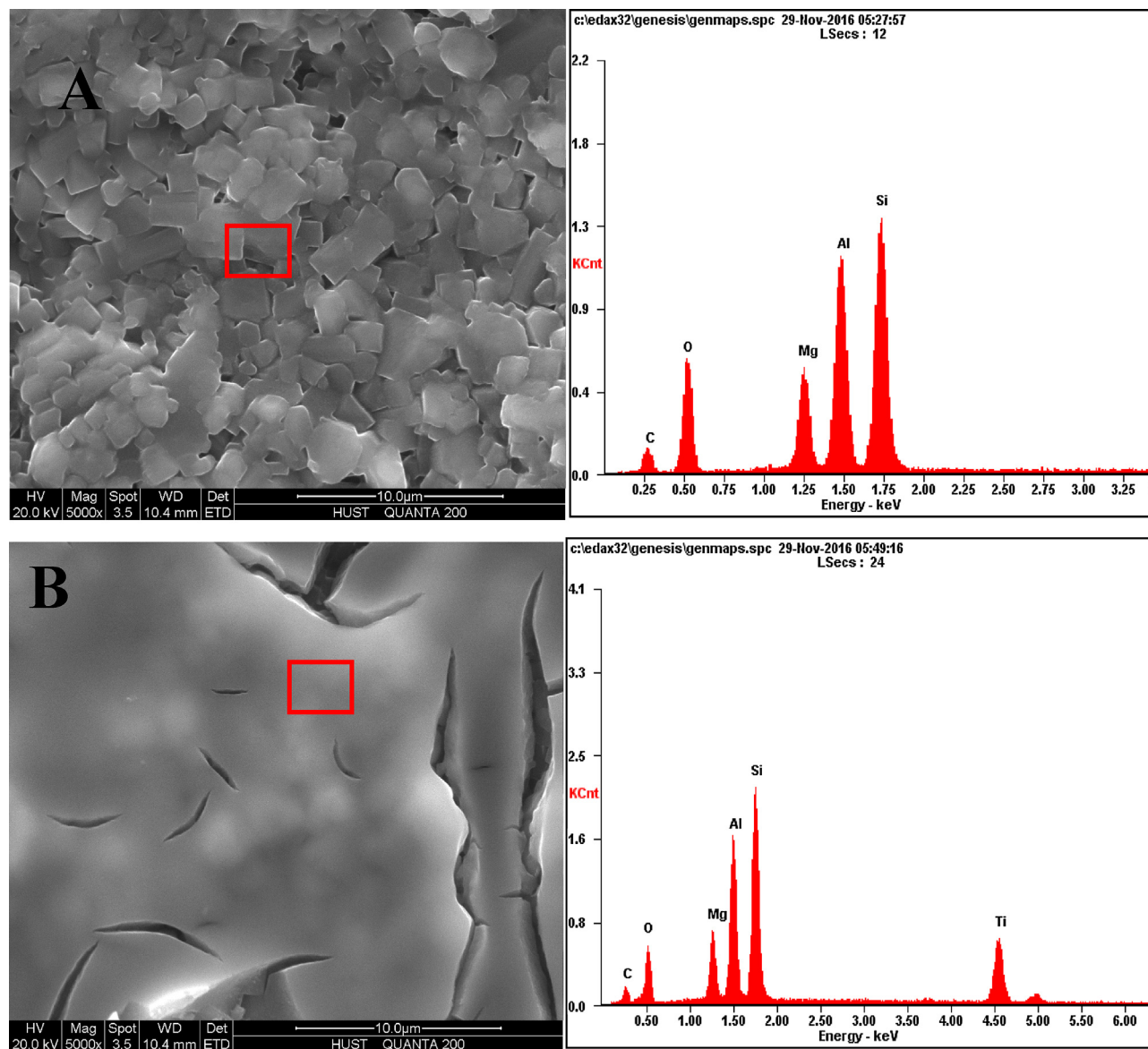

Fig. 10. SEM images and EDX analysis of honeycomb ceramics without coating (A) and coated with pristine TiO$_2$ (B).

Table 2
Photocatalytic activity and quantum efficiency of the catalysts in the internal-illuminated honeycomb photoreactor.

Samples	Catalyst loading/g[a]	CO /μmol g^{-1} h^{-1}	CH$_4$ /μmol g^{-1} h^{-1}	H$_2$ /μmol g^{-1} h^{-1}	Φ_{CO}[b] /%	Φ_{CH4} /%	Φ_{H2} /%	Φ_{total}[c] /%
Pristine TiO$_2$	0.41	0.92	0.11	0.06	0.004	0.009	0.001	0.014
V3T	0.40	1.94	0.14	0.22	0.040	0.012	0.005	0.057
W3T	0.56	1.71	0.15	0.22	0.035	0.012	0.005	0.052
V3W3T	0.32	1.91	0.22	0.27	0.039	0.018	0.006	0.063

[a] Catalyst loading was measured from the difference between the weight of the honeycomb ceramic with and without coating.

[b] Quantum efficiency(Φ) = numbers of electrons (n) × moles of yield of products/moles of photons reached the catalyst, n represents 8 for CH$_4$ and 2 for CO and H$_2$.

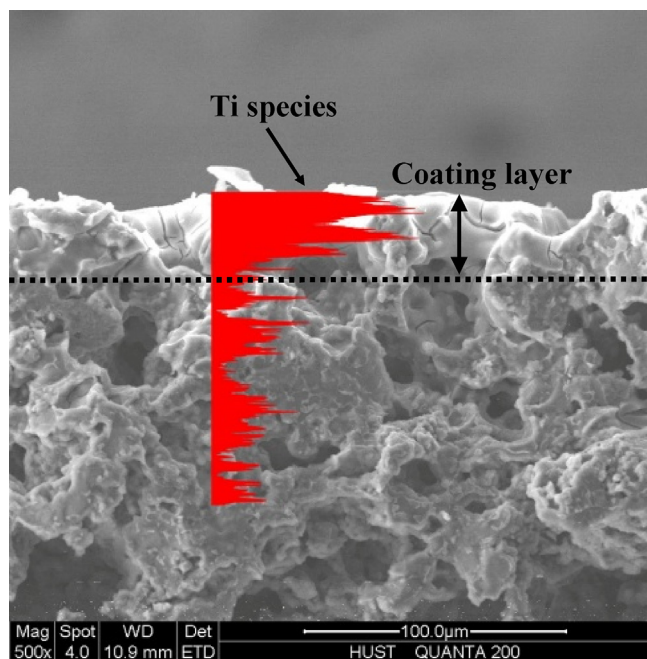[c] $\Phi_{total} = \Phi_{CO} + \Phi_{CH4} + \Phi_{H2}$.

Fig. 11. SEM images and line EDX analysis of the cross-section of the TiO$_2$ coating layer on the honeycomb ceramic.
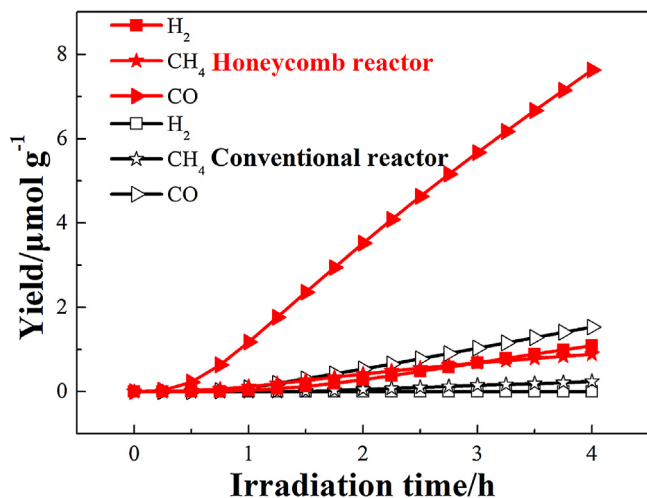

Fig. 12. Photocatalytic CO2 reduction activity of V3W3T catalyst in the honeycomb reactor and conventional reactor.

Fig. 13. CO (A) and CH$_4$ (B) and H$_2$ (C) yields of the catalysts.

the samples and both V and W doping enhanced the production of H$_2$, CO, and CH$_4$. The highest photocatalytic activity was obtained by V3W3T, whose CO, CH$_4$, and H$_2$ yields were 1.91, 0.22, and 0.27 μmol g^{-1} h^{-1}, respectively. There is no doubt that the large surface area of V3W3T is helpful for the high photocatalytic activity. However, the quantum efficiency of V3W3T is only 4.5 times as many as that of pristine TiO$_2$ while the BET surface area of the former is almost 13 times as many as that of the latter. Moreover, the photocatalytic activity of W3T is smaller than that of V3T although its larger surface area than V3T. Therefore, the large surface area is not the main reason for the highest activity of V3W3T and the main reason can be the promoted charge separation caused by V and W doping and enhanced visible light absorption by V doping, as evident in PL and UV–vis analysis. The V^{4+} and W^{6+} ions doped in TiO$_2$ lattice can capture photogenerated electrons and accelerate the electron transfer within TiO$_2$ [26,27,44]. Meanwhile, the V^{5+} on the surface of TiO$_2$ can trap photogenerated electrons and
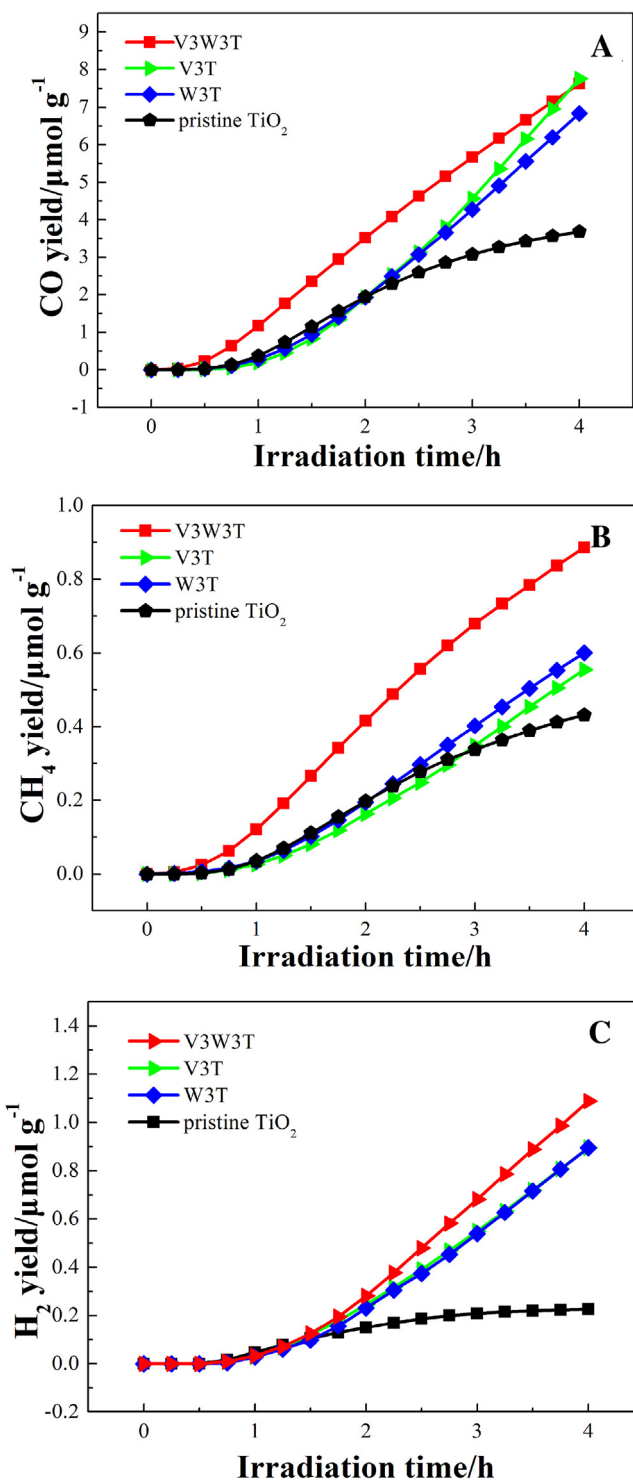
transferred them to CO$_2$ adsorbed on the surface of TiO$_2$ [26,40]. As a result, photogenerated charges were separated effectively. In addition, V^{4+} doping caused the formation of an intermediate state within the band gap of TiO$_2$ [26,27], which enables TiO$_2$ to be excited by visible light irradiation.

The quantum efficiency of the catalysts were also calculated based on the method reported in the literature [32]. The total quantum efficiency of V3W3T catalyst (0.063%) was higher than I-doped TiO$_2$ (0.0086%) [6] and Cu/TiO$_2$ nanotube (0.0266) [46] in conventional reactor and NiO/InTaO$_4$ catalyst in honeycomb reactor
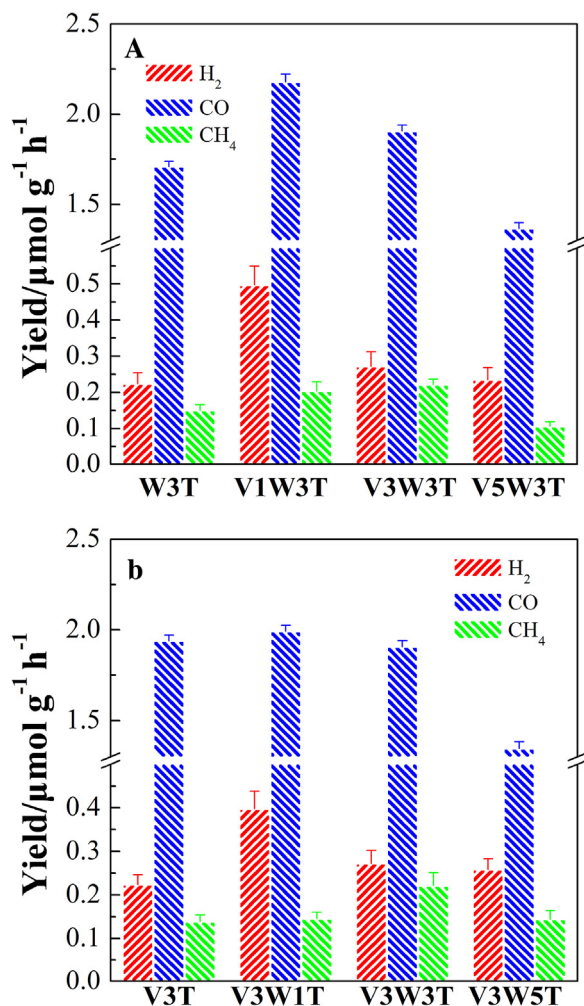
Fig. 14. Effect of V (A) and W (B) contents on the photocatalytic activity of the catalysts.

Fig. 15. Cycle performance of V3W3T catalyst in the honeycomb reactor.

(0.012%) [30], owing to the high photocatalytic activity of V and W codoped TiO_2 catalyst and high surface area and high light utilization provided by the internal-illuminated honeycomb reactor.The influence of concentration of V and W dopants on CO_2 photocatalytic reduction was also investigated. The results in Fig. 14 show that the photocatalytic activity of the samples increased first and then decreased with the increasing of V or W doping content. The optimal V and W doping concentration was 1% and 3%. This is because appropriate doping of V or W could promote the separation of photogenerated charges while excess doping of them might serve as recombination centers and accelerate charge recombination [25,47,48].

The cycle performance of V3W3T catalyst in the honeycomb reactor under simulate sunlight irradiation is exhibited in Fig. 15. After the first cycle, same experimental procedure was repeated over the spent V3W3T catalyst. The yields of CO, CH_4 and H_2 in the second and the third cycle were very close to those in the first cycle, indicating good cycle performance of V3W3T catalyst under this reaction condition. XPS was used to analyze the surface chemical states of V3W3T catalyst before and after reaction. As shown in Fig. 16, the chemical states of V and W on the surface of V3W3T catalyst were stable during photocatalytic reaction, which explains the good cycle performance of V3W3T catalyst.

A possible mechanism of CO_2 photocatalytic reaction over V and W codoped TiO_2 catalyst was proposed based on the characterization and experimental results. In the case of UV light irradiation
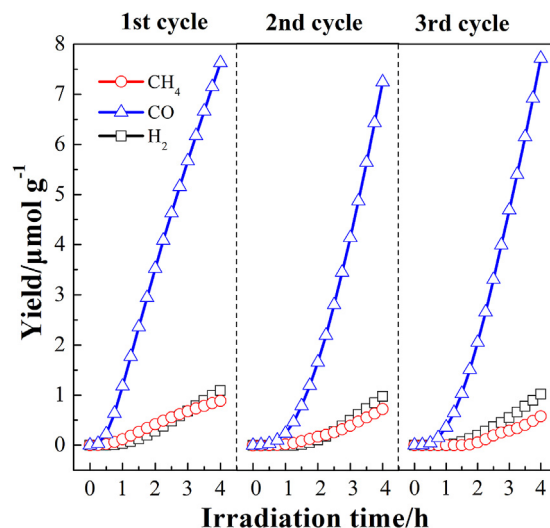
(Fig. 17A), the electrons in the VB of TiO_2 can be excited to the CB of TiO_2. Because the contact of V_2O_5 and TiO_2 can form a heterojunction and the W^{6+} doped in TiO_2 lattice can work as electron traps, the excited electrons on the CB of TiO_2 can be captured by V_2O_5 and W^{6+} [26,44] while the photogenerated holes are left in the VB of TiO_2, resulting in effective separation of photogenerated electron-hole pairs, as evident in PL analysis. Then these trapped electrons react with CO_2 and water adsorbed on the surface of the catalyst to produce solar fuels, resulting in enhanced CO_2 photocatalytic reduction.

When the V and W codoped TiO_2 catalyst is under visible light irradiation (Fig. 17B), the electrons in the valence band of TiO_2 can be excited by visible light to the intermediate state induced by V^{4+} doping, which is below the bottom of CB of TiO_2. Then the excited electrons will be trapped by V_2O_5 on the surface of TiO_2 or W^{6+} doped in the lattice of TiO_2, which ensures the effective separation of photogenerated electron-hole pair. Finally, these trapped electrons will react with the adsorbed CO_2 and water to produce hydrocarbons. Due to the enhanced visible light absorption caused by V^{4+} doping and effective separation of photogenerated charges caused by the V_2O_5 loading and W^{6+} doping, the V and W codoped TiO_2 catalyst exhibited enhanced CO_2 photocatalytic reduction activity under simulated sunlight irradiation,

4. Conclusions

In this work, V and W codoped TiO_2 catalysts were synthesized through a controlled thermal hydrolysis method and were coated on the surface of honeycomb support by using impregnation method. V and W ions doping inhibited the growth of TiO_2 grains and TiO_2 phase transformation from anatase to rutile. The V and W distributed uniformly in TiO_2 particles. V^{4+} and W^{6+} ions were doped in the lattice of TiO_2 while V^{5+} (V_2O_5) were loaded on the surface of TiO_2. V^{4+} doping enhanced the visible light absorption of TiO_2 by introducing an intermediate state within the band gap of TiO_2. The V_2O_5 on the surface of TiO_2 and W^{6+} doped in the TiO_2 lattice could trap photogenerated electrons and transfer them to CO_2 and water adsorbed on the surface TiO_2, resulting in effective separation of photogenerated charges. CO_2 photocatalytic reduction over V and W coped TiO_2 catalysts was performed in an internal-illuminated honeycomb photoreactor under simulated sunlight irradiation. The efficiency of CO_2 photocatalytic reduction in honeycomb reactor was much higher than in conven-
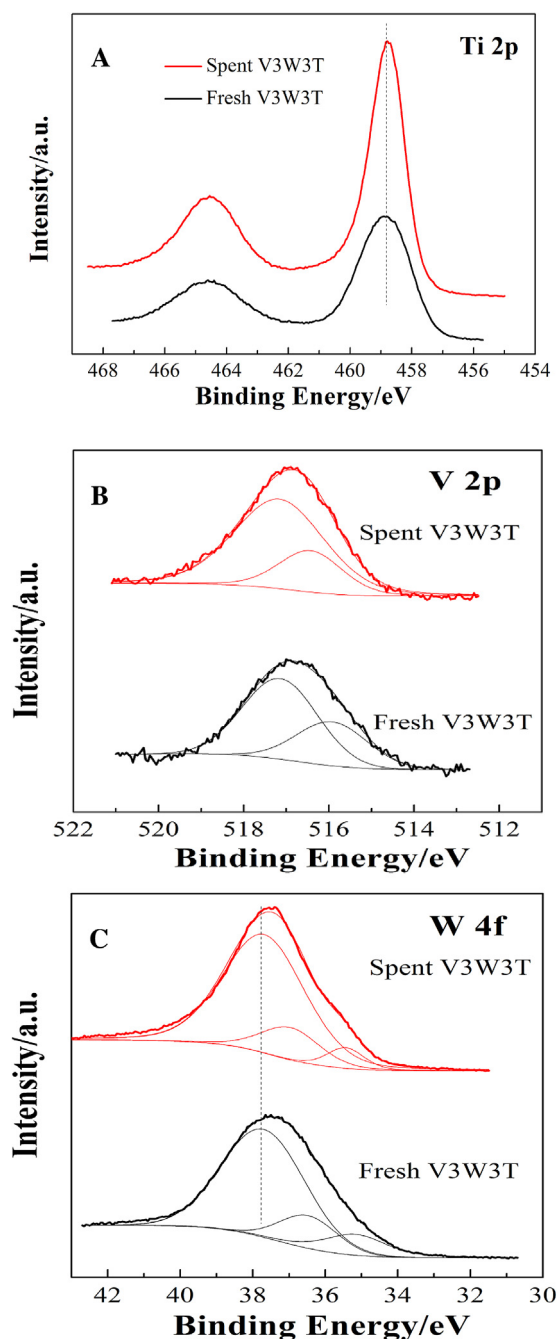
Fig. 16. Ti 2p (A), V 2p (B), and W 4f (C) XPS spectra of V3W3T catalyst before and after photocatalytic reaction.

Fig. 17. Mechanism of CO_2 photocatalytic reduction over V and W codoped TiO_2 under UV (A) and visible light (B) irradiation.

References

[1] J. Low, B. Cheng, J. Yu, Surface modification and enhanced photocatalytic CO_2 reduction performance of TiO_2: a review, Appl. Surf. Sci. 392 (2017) 658–686.

[2] Y.-H. Cheng, V.-H. Nguyen, H.-Y. Chan, J.C.S. Wu, W.-H. Wang, Photo-enhanced hydrogenation of CO_2 to mimic photosynthesis by CO co-feed in a novel twin reactor, Appl. Energy 147 (2015) 318–324.

[3] C. Gao, Q. Meng, K. Zhao, H. Yin, D. Wang, J. Guo, S. Zhao, L. Chang, M. He, Q. Li, H. Zhao, X. Huang, Y. Gao, Z. Tang, Co_3O_4 hexagonal platelets with controllable facets enabling highly efficient visible-light photocatalytic reduction of CO_2, Adv. Mater. 28 (2016) 6485–6490.

[4] T. Inoue, A. Fujishima, S. Konishi, K. Honda, Photoelectrocatalytic reduction of carbon dioxide in aqueous suspensions of semiconductor powders, Nature 277 (1979) 637–641.

[5] Z. Xiong, H. Wang, N. Xu, H. Li, B. Fang, Y. Zhao, J. Zhang, C. Zheng, Photocatalytic reduction of CO_2 on Pt^{2+}–Pt^0/TiO_2 nanoparticles under UV/Vis light irradiation: a combination of Pt^{2+} doping and Pt nanoparticles deposition, Int. J. Hydrogen Energy 40 (2015) 10049–10062.

[6] Q. Zhang, Y. Li, E.A. Ackerman, M. Gajdardziska-Josifovska, H. Li, Visible light responsive iodine-doped TiO_2 for photocatalytic reduction of CO_2 to fuels, Appl. Catal. A: Gen. 400 (2011) 195–202.

tional reactor due to the high surface area per unit volume and efficient utilization of light in the honeycomb reactor. Appropriate doping of V and W could effectively enhance the activity of TiO_2. The CO, CH_4, and H_2 yields of V3W3T catalyst were 1.91, 0.22, and 0.27 μmol g^{-1} h^{-1}, respectively, which were much higher than those of pristine TiO_2 and single metal doped TiO_2 catalysts. The V and W codoped TiO_2 catalyst exhibited enhanced photocatalytic activity comparing with pristine TiO_2 and single metal doped TiO_2 catalysts, which could be attributed to the enhanced visible light absorption and promoted separation of photogenerated electron-hole pairs caused by V and W codoping. The V and W codoped TiO_2 also exhibited good cycle performance due to the stable chemical states of V and W during photocatalytic reaction.
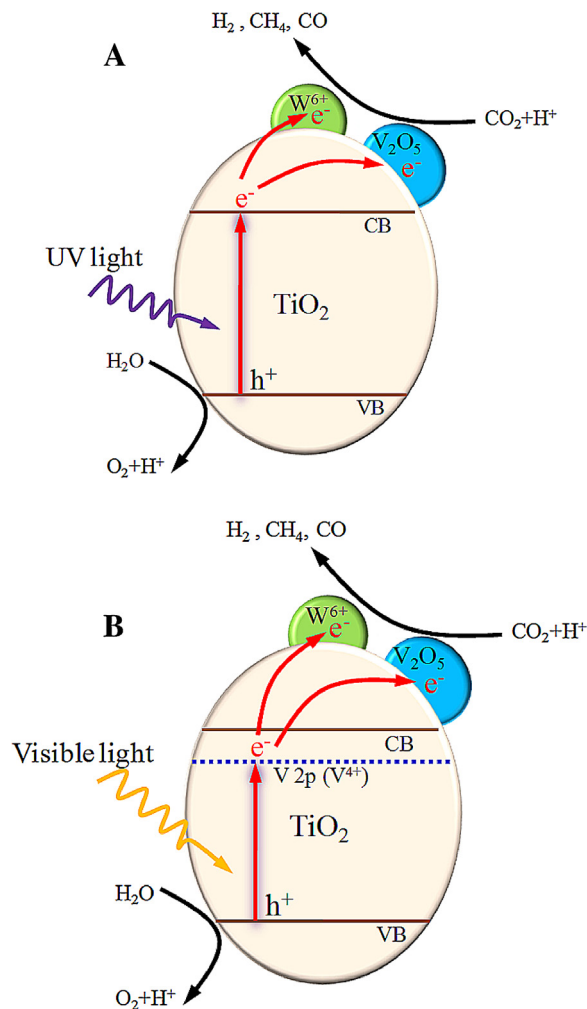
[7] Z. Xiong, Y. Luo, Y. Zhao, J. Zhang, C. Zheng, J.C. Wu, Synthesis, characterization and enhanced photocatalytic CO_2 reduction activity of graphene supported TiO_2 nanocrystals with coexposed {001} and {101} facets, Phys. Chem. Chem. Phys. 18 (2016) 13186–13195.

[8] V. Etacheri, R. Roshan, V. Kumar, Mg-doped ZnO nanoparticles for efficient sunlight-driven photocatalysis, ACS Appl. Mater. Interfaces 4 (2012) 2717–2725.

[9] Z. Xiong, Z. Lei, Z. Xu, X. Chen, B. Gong, Y. Zhao, H. Zhao, J. Zhang, C. Zheng, Flame spray pyrolysis synthesized ZnO/CeO_2 nanocomposites for enhanced CO_2 photocatalytic reduction under UV–Vis light irradiation, J. CO_2 Util. 18 (2017) 53–61.

[10] J. Zhao, Y. Wang, Y. Li, X. Yue, C. Wang, Phase-dependent enhancement for CO_2 photocatalytic reduction over CeO_2/TiO_2 catalysts, Catal. Sci. Technol. 6 (2016) 7967–7975.

[11] Y. Wang, B. Li, C. Zhang, L. Cui, S. Kang, X. Li, L. Zhou, Ordered mesoporous CeO_2-TiO_2 composites: highly efficient photocatalysts for the reduction of CO_2 with H_2O under simulated solar irradiation, Appl. Catal. B: Environ. 130–131 (2013) 277–284.

[12] J. Fu, B. Zhu, C. Jiang, B. Cheng, W. You, J. Yu, Hierarchical porous O-doped g-C_3N_4 with enhanced photocatalytic CO_2 reduction activity, Small 13 (2017).

[13] Y.P. Xie, G. Liu, L. Yin, H.-M. Cheng, Crystal facet-dependent photocatalytic oxidation and reduction reactivity of monoclinic WO_3 for solar energy conversion, J. Mater. Chem. 22 (2012) 6746–6751.

[14] X. Chen, Y. Zhou, Q. Liu, Z. Li, J. Liu, Z. Zou, Ultrathin, single-crystal WO_3 nanosheets by two-dimensional oriented attachment toward enhanced photocatalystic reduction of CO_2 into hydrocarbon fuels under visible light, ACS Appl. Mater. Interfaces 4 (2012) 3372–3377.

[15] Z. Xiong, Z. Lei, C.-C. Kuang, X. Chen, B. Gong, Y. Zhao, J. Zhang, C. Zheng, J.C.S. Wu, Selective photocatalytic reduction of CO_2 into CH_4 over Pt-Cu_2O TiO_2 nanocrystals: the interaction between Pt and Cu_2O cocatalysts, Appl. Catal. B: Environ. 202 (2017) 695–703.

[16] Z. Xiong, Y. Zhao, J. Zhang, C. Zheng, Efficient photocatalytic reduction of CO_2 into liquid products over cerium doped titania nanoparticles synthesized by a sol–gel auto-ignited method, Fuel Process. Technol. 135 (2015) 6–13.

[17] W.N. Wang, W.J. An, B. Ramalingam, S. Mukherjee, D.M. Niedzwiedzki, S. Gangopadhyay, P. Biswas, Size and structure matter: enhanced CO_2 photoreduction efficiency by size-resolved ultrafine Pt nanoparticles on TiO_2 single crystals, J. Am. Chem. Soc. 134 (2012) 11276–11281.

[18] I.H. Tseng, J.C.S. Wu, H.-Y. Chou, Effects of sol–gel procedures on the photocatalysis of Cu/TiO_2 in CO_2 photoreduction, J. Catal. 221 (2004) 432–440.

[19] Q. Zhang, T. Gao, J.M. Andino, Y. Li, Copper and iodine co-modified TiO_2 nanoparticles for improved activity of CO_2 photoreduction with water vapor, Appl. Catal. B: Environ. 123–124 (2012) 257–264.

[20] W. Wang, D. Xu, B. Cheng, J. Yu, C. Jiang, Hybrid carbon@TiO_2 hollow spheres with enhanced photocatalytic CO_2 reduction activity, J. Mater. Chem. A 5 (2017) 5020–5029.

[21] M.S. Akple, J. Low, Z. Qin, S. Wageh, A.A. Al-Ghamdi, J. Yu, S. Liu, Nitrogen-doped TiO_2 microsheets with enhanced visible light photocatalytic activity for CO_2 reduction, Chin. J. Catal. 36 (2015) 2127–2134.

[22] M. Tahir, N.S. Amin, Photocatalytic CO_2 reduction with H_2 as reductant over copper and indium co-doped TiO_2 nanocatalysts in a monolith photoreactor, Appl. Catal. A: Gen. 493 (2015) 90–102.

[23] J.C.S. Wu, C.-H. Chen, A visible-light response vanadium-doped titania nanocatalyst by sol–gel method, J. Photochem. Photobiol. A: Chem. 163 (2004) 509–515.

[24] M. Tahir, N.S. Amin, Indium-doped TiO_2 nanoparticles for photocatalytic CO_2 reduction with H_2O vapors to CH_4, Appl. Catal. B: Environ. 162 (2015) 98–109.

[25] Q. Xiao, L. Gao, One-step hydrothermal synthesis of C, W-codoped mesoporous TiO_2 with enhanced visible light photocatalytic activity, J. Alloys Compd. 551 (2013) 286–292.

[26] J. Liu, R. Han, Y. Zhao, H. Wang, W. Lu, T. Yu, Y. Zhang, Enhanced photoactivity of V-N codoped TiO_2 derived from a two-step hydrothermal procedure for the degradation of PCP-Na under visible light irradiation, J. Phys. Chem. C 115 (2011) 4507–4515.

[27] T.-D. Pham, B.-K. Lee, Selective removal of polar VOCs by novel photocatalytic activity of metals co-doped TiO_2/PU under visible light, Chem. Eng. J. 307 (2017) 63–73.

[28] Y.-F. Li, D. Xu, J.I. Oh, W. Shen, X. Li, Y. Yu, Mechanistic study of codoped titania with nonmetal and metal ions: a case of C + Mo codoped TiO_2, ACS Catal. 2 (2012) 391–398.

[29] Y. Yuan, Y. Zhao, H. Li, Y. Li, X. Gao, C. Zheng, J. Zhang, Electrospun metal oxide-TiO_2 nanofibers for elemental mercury removal from flue gas, J. Hazard. Mater. 227-228 (2012) 427–435.

[30] P.-Y. Liou, S.-C. Chen, J.C.S. Wu, D. Liu, S. Mackintosh, M. Maroto-Valer, R. Linforth, Photocatalytic CO_2 reduction using an internally illuminated monolith photoreactor, Energy Environ. Sci. 4 (2011) 1487–1494.

[31] K.-T. Lu, V.-H. Nguyen, Y.-H. Yu, C.-C. Yu, J.C.S. Wu, L.-M. Chang, A.Y.-C. Lin, An internal-illuminated monolith photoreactor towards efficient photocatalytic degradation of ppb-level isopropyl alcohol, Chem. Eng. J. 296 (2016) 11–18.

[32] O. Ola, M. Maroto-Valer, D. Liu, S. Mackintosh, C.-W. Lee, J.C.S. Wu, Performance comparison of CO_2 conversion in slurry and monolith photoreactors using Pd and Rh-TiO_2 catalyst under ultraviolet irradiation, Appl. Catal. B: Environ. 126 (2012) 172–179.

[33] M. Tahir, N.S. Amin, Performance analysis of nanostructured NiO–In_2O_3/TiO_2 catalyst for CO_2 photoreduction with H_2 in a monolith photoreactor, Chem. Eng. J. 285 (2016) 635–649.

[34] M. Gurulakshmi, M. Selvaraj, A. Selvamani, P. Vijayan, N.R. Sasi Rekha, K. Shanthi, Enhanced visible-light photocatalytic activity of V_2O_5/S-TiO_2 nanocomposites, Appl. Catal. A: Gen. 449 (2012) 31–46.

[35] E.O. Oseghe, P.G. Ndungu, S.B. Jonnalagadda, Photocatalytic degradation of 4-chloro-2-methylphenoxyacetic acid using W-doped TiO_2, J. Photochem. Photobiol. A: Chem. 312 (2015) 96–106.

[36] B. Wang, G. Zhang, X. Leng, Z. Sun, S. Zheng, Characterization and improved solar light activity of vanadium doped TiO_2/diatomite hybrid catalysts, J. Hazard. Mater. 285 (2015) 212–220.

[37] J.H. Pan, W.I. Lee, Preparation of highly ordered cubic mesoporous WO_3/TiO_2 films and their photocatalytic properties, Chem. Mater. 18 (2006) 847–853.

[38] L. Zhang, R.V. Koka, A study on the oxidation and carbon diffusion of TiC in alumina–titanium carbide ceramics using XPS and Raman spectroscopy, Mater. Chem. Phys. 57 (1998) 23–32.

[39] B. Fang, N.K. Chaudhari, M.-S. Kim, J.H. Kim, J.-S. Yu, Homogeneous deposition of platinum nanoparticles on carbon black for proton exchange membrane fuel cell, J. Am. Chem. Soc. 131 (2009) 15330–15338.

[40] T.-D. Pham, B.-K. Lee, Novel photocatalytic activity of Cu@V co-doped TiO_2/PU for CO_2 reduction with H_2O vapor to produce solar fuels under visible light, J. Catal. 345 (2017) 87–95.

[41] X. Yang, F. Ma, K. Li, Y. Guo, J. Hu, W. Li, M. Huo, Y. Guo, Mixed phase titania nanocomposite codoped with metallic silver and vanadium oxide: new efficient photocatalyst for dye degradation, J. Hazard. Mater. 175 (2010) 429–438.

[42] L. Li, C.-y. Liu, Y. Liu, Study on activities of vanadium (IV/V) doped $TiO_2(R)$ nanorods induced by UV and visible light, Mater. Chem. Phys. 113 (2009) 551–557.

[43] C. Belver, C. Han, J.J. Rodriguez, D.D. Dionysiou, Innovative W-doped titanium dioxide anchored on clay for photocatalytic removal of atrazine, Catal. Today 280 (2017) 21–28.

[44] J. Gong, C. Yang, W. Pu, J. Zhang, Liquid phase deposition of tungsten doped TiO_2 films for visible light photoelectrocatalytic degradation of dodecyl-benzenesulfonate, Chem. Eng. J. 167 (2011) 190–197.

[45] L. Liu, H. Zhao, J.M. Andino, Y. Li, Photocatalytic CO_2 reduction with H_2O on TiO_2 nanocrystals: comparison of anatase, rutile, and brookite polymorphs and exploration of surface chemistry, ACS Catal. 2 (2012) 1817–1828.

[46] O.K. Varghese, M. Paulose, T. LaTempa, C.A. Grimes, High-rate solar photocatalytic conversion of CO_2 and water vapor to hydrocarbon fuels, Nano Lett. 9 (2008) 731–737.

[47] O. Ola, M.M. Maroto-Valer, Synthesis, characterization and visible light photocatalytic activity of metal based TiO_2 monoliths for CO_2 reduction, Chem. Eng. J. 283 (2016) 1244–1253.

[48] S. Sathasivam, D.S. Bhachu, Y. Lu, N. Chadwick, S.A. Althabaiti, A.O. Alyoubi, S.N. Basahel, C.J. Carmalt, I.P. Parkin, Tungsten doped TiO_2 with enhanced photocatalytic and optoelectrical properties via aerosol assisted chemical vapor deposition, Sci. Rep. 5 (2015) 10952.